Interactions Between Friction Modifiers and Dispersants in Lubricants: The Case of Glycerol Monooleate and Polyisobutylsuccinimide-Polyamine

Interactions Between Friction Modifiers and Dispersants in Lubricants: The Case of Glycerol Monooleate and Polyisobutylsuccinimide-Polyamine

Georgia Tsagkaropoulou,[†] Chris P. Warrens,[‡] and Philip J. Camp[*,†]

†*School of Chemistry, University of Edinburgh, David Brewster Road, Edinburgh EH9 3FJ, Scotland*

‡*Research and Technology Fuels and Lubricants, BP International Limited, Technology Centre, Whitchurch Hill, Pangbourne, Reading RG8 7QR, England*

E-mail: philip.camp@ed.ac.uk

June 4, 2019

Abstract

The structural and frictional properties of 10 wt% solutions of the amphiphilic molecules glycerol monooleate (GMO) and polyisobutylsuccinimide-polyamine (PIBSA-PAM) in squalane are studied using molecular dynamics simulations in bulk and under confinement between iron-oxide surfaces. GMO is a friction modifier, PIBSA-PAM is a dispersant, and squalane is a good model for typical base oils. A range of liquid compositions and applied pressures is explored and the formation and stability of reverse micelles is determined under quiescent and shear conditions. Micellization is observed mainly in systems with a high GMO content, but PIBSA-PAM may also form small aggregates on its own. In the confined systems under both static and shear conditions, some surfactant molecules adsorb onto the surfaces, with the rest of the molecules forming micelles or aggregates. Shearing the liquid layer under high pressure causes almost all of the micelles and aggregates to break, except in systems with around 7.5 wt% GMO and 2.5 wt% PIBSA-PAM. The presence of micelles and adsorbed surfactants is found to be correlated with a low kinetic friction coefficient, and hence there is an optimum composition range for friction reduction. This work highlights the importance of cooperative interactions between lubricant additives.

Keywords

adsorption; friction; liquid-solid interface; lubrication; molecular simulations; self-assembly

1 Introduction

Lubrication is essential in the automotive industry, as it enhances the performance and lifetime of engines, and reduces fuel consumption and environmental impacts. The properties of lubricants are controlled by additives which are designed for various purposes and comprise approximately 20 wt% of the liquid, with the remaining 80 wt% being the base oil. Examples of additive types include antiwear agents, friction modifiers, dispersants, detergents, viscosity modifiers, antioxidants, corrosion inhibitors, and extreme-pressure additives. Many of these additives are surface-active agents, or surfactants, which are essentially compounds that adsorb at the interfaces between polar surfaces and the non-polar base oil. In this work, the interplay between micellization, adsorption, and friction at the solid-liquid interface will be investigated for two types of lubricant additives, a friction modifier and a dispersant. In the classical picture of friction modification, surfactant-type molecules adsorb on inorganic surfaces in contact with base oil, providing monolayer coverage, and a deformable barrier between two such surfaces close to contact.[1–3] Dispersants are molecules that solubilize combustion products such as soot, sludge, and other contaminants that would otherwise form deposits on moving parts of the engine and trigger wear and corrosion. By preventing aggregation, any soot-induced viscosity effects are minimized, deposition and oxidation are reduced, and therefore localized heating is avoided.[4,5]

Although a lot is known about the performance of each type of molecule in isolation, less is known about the cooperative and/or antagonistic molecular-scale interactions between them. This is the focus of the current work. There are four fundamental processes that involve surfactant compounds: micellization; dissolution of the surfactants; solubilization by surfactants; and interfacial processes.[4] Typically, these compounds consist of one or more oleophilic hydrocarbon tails and a polar head group or connecting unit. When dispersed in

non-polar media, the attractive interactions between the polar groups, and packing of the non-polar tails, dictate the size and shape of the resulting reverse micelle. The polar groups also attract contaminants and enclose them in the micelles, thus preventing deposition onto surfaces. The micelles are then carried away by the oil until they are removed by a filter. Adsorption at solid-liquid interfaces, driven by the polar groups, is also an important process which controls friction and wear. Therefore, it is important to understand the competition between micellization and adsorption of amphiphilic molecules, and its tribological effects. The interactions between different additives increase the complexity of the problem, but given that lubricant formulations may contain a dozen different additive types, it is essential to start working towards a holistic view of what is a very complicated system.

Molecular dynamics (MD) simulations provide unique insights on the molecular-scale structure and dynamics in complex fluids. Previous simulation work on lubrication has focused primarily on a single type of additive in a simple model base oil, and has been reviewed recently.[6] Examples include polymers and hydrocarbons,[7–15] silanes,[16] fatty acids, amines, amides, and esters[13,17–25] glycerin,[26] glycerides,[22,27] zinc dialkyldithiophosphates,[28] molybdenum sulfides,[29,30] room-temperature ionic liquids,[31,32] and carbon nanoparticles.[33]

The additives studied in this work are glycerol monooleate (GMO, RMM = 356.55 g mol^{-1}), a widely used friction modifier, and polyisobutylsuccinimide-polyamine (PIBSA-PAM, RMM = 549.89 g mol^{-1}), which is an ashless, polymeric dispersant. The molecular structures are shown in Figure 1 (a) and (b). GMO is known to form normal micelles in water[34] and reverse micelles in non-aqueous solvents.[35–38] The self-assembly of GMO in bulk solution has been thoroughly investigated using MD simulations and small-angle neutron scattering by Bradley-Shaw *et al.*[39] MD simulations have also been used to study the structure, dynamics, and friction of GMO in simple organic solvents confined and sheared between

mica surfaces.[40] The effects of GMO hydrolysis on the self-assembly, adsorption, and friction have also been explored.[41] As an ashless dispersant, PIBSA-PAM is not expected to form compact micelles, but aggregates with a small aggregation number ($n < 10$) might be observed;[4] in some PIBSA-based dispersants, this self-assembly competes with surface adsorption at high concentrations.[42] A single model compound, squalane (2,6,10,15,19,23-hexamethyltetracosane, RMM = 422.83 g mol^{-1}) is used to simulate the base oil of the lubricant; the molecular structure is shown in Figure 1(c). Squalane is a branched hydrocarbon with a long backbone, with physical and chemical properties that are close to those of a typical engine lubricant base oil.[43] The simplicity of its structure and its physical similarities with real base oils make squalane a good choice as a model compound. The GMO and PIBSA-PAM additives may be referred to as 'surfactants' and the squalane as the 'solvent'. To study the effects of confinement and shear, the liquid is placed as a layer between parallel iron-oxide (hematite, α-Fe_2O_3) surfaces. Iron oxide can be considered a reasonable model of the oxidized surfaces of engine components, which are often made from steel. It is convenient from an experimental point of view, as it can be used as a powder for adsorption work, or sputtered onto substrates for reflectivity and surface-spectroscopy measurements. Therefore, Fe_2O_3 is used in many experimental and computational studies of adsorption[44–48] and friction[13,24] in oil-based systems.

The rest of this article is organized as follows. The simulation methods are summarized in Section 2. The results are presented for bulk liquids (Section 3.1), confined liquids under static conditions (Section 3.2), and confined liquids under shear conditions (Section 3.3). Conclusions are presented in Section 4.

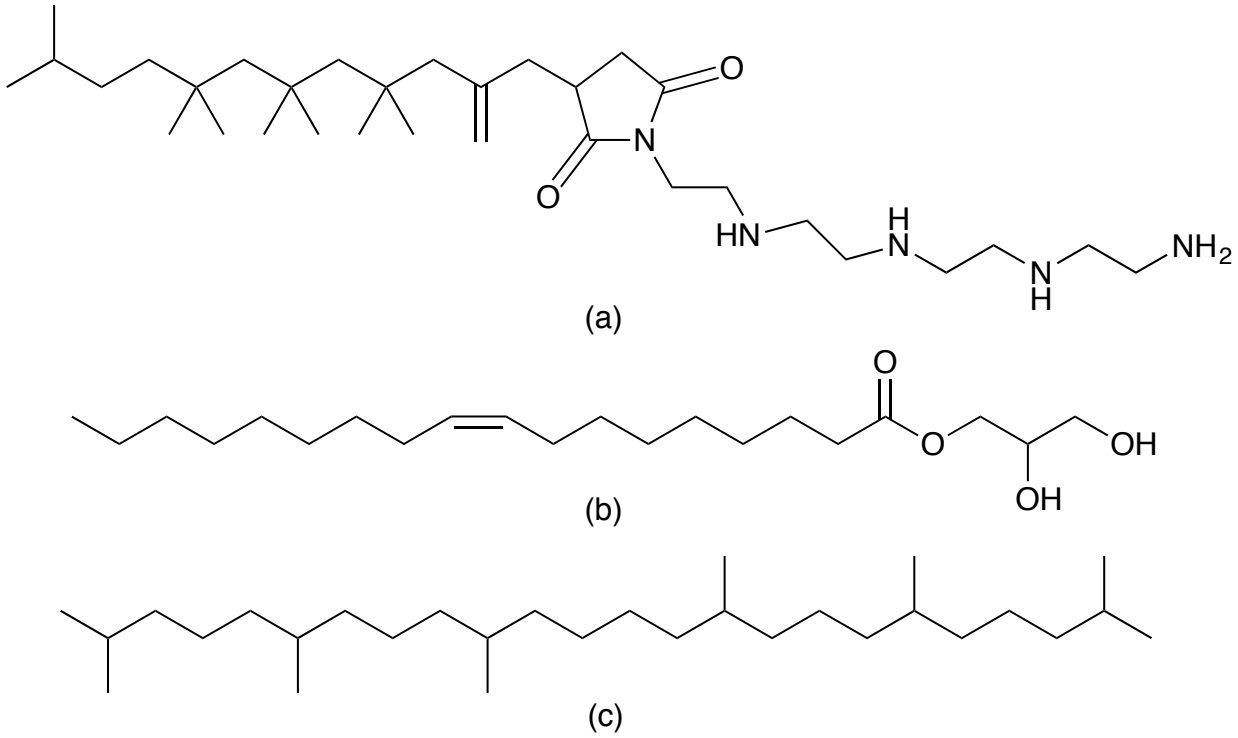

Figure 1: The structures of the compounds used in this work: (a) polyisobutylsuccinimide-polyamine (PIBSA-PAM), a dispersant; (b) glycerol monooleate (GMO), a friction modifier; and (c) squalane, a branched hydrocarbon that simulates bulk oil.

2 Methods

Initially, systems with five different compositions were studied, with 10 wt% additive overall, and GMO contents of 0.0, 2.5, 5.0, 7.5, and 10.0 wt%. Some additional simulations were done at compositions of 6.25 wt% and 8.75 wt% GMO to check a hypothesis about the dependence of friction coefficient on composition – see Section 3.3. The numbers of molecules, and other details, are given in Table 1. The total additive content is higher than is found in bulk lubricant formulations, but solvent 'squeeze out' from between surfaces can lead to higher local concentrations of additive, particularly if the additive can adsorb onto the surfaces.[49,50] Therefore, in the simulations, a high concentration was used so that there was sufficient

surface coverage and/or aggregate content to cause more pronounced trends in the observed friction, over and above the lubricating effect of the solvent itself. Moreover, it is convenient experimentally to study bulk liquids with high additive content. For example, reverse-micelle formation in 10 wt% solutions of GMO in n-heptane was studied using small-angle neutron scattering, with the high additive concentration leading to better signal detection.[21]

All-atom MD simulations were performed using LAMMPS.[51,52] Interactions were taken from the OPLS-AA forcefield.[53,54] This forcefield was used in earlier studies on GMO self-assembly in C_7 hydrocarbons, and the agreement between the reverse-micelle sizes from MD simulation (radius of gyration, $R_g = 15.5$ Å) and small-angle neutron scattering experiments ($R_g = 16.6$ Å) was good. Some preliminary MD simulations of squalane at $P = 1$ atm and $T = 298.15$ K gave a density of 840 kg m^{-3}, just 4% higher than the experimental value.[55] The Ewald particle-particle particle-mesh method was used to compute the long-range electrostatic interactions. The equations of motion were integrated using the velocity-Verlet algorithm with a time step of 1 fs.

Bulk liquids were studied in a cubic simulation cell with periodic boundary conditions applied in all three directions. The solvent and surfactants were placed in random configurations in a cubic box of side 100 Å. First, NVE dynamics were run for 0.5 ns to relax the molecules, and then the system was equilibrated in the NPT ensemble for 10 ns at $P = 1$ atm and $T = 298.15$ K. The simulation was then switched to the NVT ensemble for a production run of 100 ns under the same conditions. The temperature and pressure were controlled with a Nosé-Hoover thermostat and barostat.

Confined liquids were studied between parallel (100) surfaces of iron (III) oxide, α-Fe_2O_3 (hematite).[56] Each slab consisted of 2400 atoms, with lateral (xy) dimensions of 55.09 Å $\times$ 50.38 Å and thickness (z) of 8.61 Å. The surface interactions were calculated with Lennard-

Table 1: Composition and structural characterization of systems at $P = 1$ atm. N_{PP} is the number of PIBSA-PAM molecules in the system, N_{G} is the number of GMO molecules in the system, N_{sq} is the number of squalane molecules in the system, and N_{atom} is the total number of atoms in the liquid layer. The composition and radius of gyration R_{g} of each micelle is given under static conditions in bulk at $T = 298.15$ K. $\mathrm{G}_m\mathrm{PP}_n$ means a single aggregate containing m GMO molecules and n PIBSA-PAM molecules. Note that with 10 wt% GMO, there were two aggregates.

wt%(PP)	wt%(G)	N_{PP}	N_{G}	N_{sq}	N_{atom}	aggregate	R_{g}/Å
10.00	0.00	30	0	350	35260	none	
7.50	2.50	23	12	350	35326	none	
5.00	5.00	15	23	350	35225	$\mathrm{G_4PP_5}$	27.5(2)
3.75	6.25	11	29	350	35207	$\mathrm{G_9PP_3}$	21.7(2)
2.50	7.50	8	35	350	35291	$\mathrm{G_8PP_2}$	22.4(5)
1.25	8.75	4	40	350	35208	$\mathrm{G_{17}PP_2}$	27.0(2)
0.00	10.00	0	46	350	35190	$\mathrm{G_{13}}$	15.1(2)
						$\mathrm{G_{11}}$	19.2(4)

Jones and Coulomb potentials, as developed by Berro *et al.*[28] Although these types of force fields are strictly limited to describing physisorption, good agreement between experiments can be found, even for organic acids[25] and bases.[21] To prevent the surface from warping while maintaining flexibility and allowing thermostatting, harmonic bonds were inserted between neighboring atoms within 3 Å of one another with a force constant of 130 kcal mol^{-1} $\mathrm{Å}^{-2}$, as used by Berro *et al.*[28] Periodic boundary conditions were applied in the xy directions only, and the corresponding box lengths were held constant and commensurate with the slab dimensions. Fixed-load conditions were simulated by maintaining constant forces in the z direction on the outermost layers of atoms in the iron-oxide slabs, equivalent to a desired pressure. Shear conditions were simulated by moving the slabs with equal and opposite sliding velocities in the x direction, given by $\pm\frac{1}{2}v_{\mathrm{s}}$, where $v_{\mathrm{s}} = 0.5$, 1, 2, 5, 10, and 20 m s^{-1}. The temperature was controlled by applying a Nosé-Hoover thermostat in the y direction only, so as not to disrupt the velocity profile in the xz plane. The simulation

protocol was as follows. First, the surfactants and solvent were randomly mixed in various ratios in a cuboidal box and then confined between the two iron-oxide slabs at a surface separation of at least $H = 110$ Å, with $z = 0$ and $z = H$ being defined as the positions of the innermost layers of iron atoms in the slabs. Then a fixed load corresponding to $P = 1$ atm was applied, and constant-temperature dynamics at $T = 313$ K were run for 100 ns to equilibrate the system. This length of run was chosen to ensure that the liquid mass density and the surface separation H had plateaued, and that any self-assembly processes had reached completion; this usually takes no longer than 25 ns.[39] Some runs were also carried out at $P = 10^3$ atm and 10^4 atm. Finally, the temperature and pressure were raised to $T = 353$ K and $P = 10^3$ atm, respectively, and the iron-oxide slabs were given constant sliding velocities $\pm\frac{1}{2}v_\mathrm{s}$ to simulate the high-temperature, high-pressure, and shear conditions typically found in engines. Some runs were also carried out at $P = 10^4$ atm. A steady state was established under shear conditions over about 10 ns (shear accelerates the approach to the steady state) and then a production run of 60 ns was carried out. Mass-density profiles, the shear rate $\dot{\gamma} = v_\mathrm{s}/H$, the velocity profile $v_x(z)$, and the kinetic friction coefficient μ were calculated and averaged over the production run. The friction coefficient was calculated using the extended Amontons-Coulomb law $F_\mathrm{L} = F_0 + \mu F_\mathrm{N}$, where F_L and F_N are the average total lateral and normal forces acting on the sliding walls, respectively, and F_0 is the Derjaguin offset that represents adhesive surface forces. At high pressure, $F_\mathrm{N} \gg F_0$, and hence the kinetic friction coefficient can be calculated using $\mu \approx F_\mathrm{L}/F_\mathrm{N}$ to good precision.[21] F_L and F_N were calculated, respectively, as the averages of the x and z components of the vector sum of all forces acting on the surface atoms due to the liquid layer. These quantities underwent large fluctuations, and the instantaneous values could be positive or negative. The average values of F_L and F_N were used to calculate μ, and the error bar was computed

by propagating the standard errors $s = \sigma/\sqrt{n}$ based on one standard deviation σ, where n is the number of independent readings. The instantaneous forces were computed every 50 fs over the production run, which typically took about 7 days on 96 cores using the BP HPC facility.

3 Results and discussion

3.1 Self-assembly in the bulk liquid

Figure 2 shows snapshots of five systems with GMO contents ranging from 0.0 wt% to 10.0 wt%. The GMO and PIBSA-PAM molecules are colored differently. As a general rule, the degree of association between additive molecules increases with increasing GMO content. PIBSA-PAM, by itself, forms small, short-lived clusters, while pure GMO is well known to form reverse micelles.[35–41] Nonetheless, with 2.5 wt% PIBSA-PAM and 7.5 wt% GMO, there is evidence of significant mixed clusters. Where possible, aggregates were identified by visualizing the generated trajectories using VMD software[57] during the production run, and the number of molecules of each additive, and the radius of gyration R_{g}, were determined. R_{g} was calculated by finding the dimensions of a uniformly dense ellipsoid with the same mass and inertia tensor of an aggregate. The inertia tensor is given by

$$\mathbf{I} = \sum_{i=1}^{n} m_i \left[(\mathbf{r}_i \cdot \mathbf{r}_i)\mathbf{1} - \mathbf{r}_i \otimes \mathbf{r}_i \right] \tag{1}$$

where m_i and $\mathbf{r}_i$ are, respectively, the mass and position vector of atom i, and n is the number of atoms in the aggregate. Diagonalizing $\mathbf{I}$ yields the eigenvalues $I_a > I_b > I_c$, these being the moments of inertia of the aggregate. The corresponding eigenvectors are the principal

axes. The radius of gyration of a uniformly dense ellipsoid with the same principal axes is given by

$$R_{\mathrm{g}}^2 = \frac{I_a + I_b + I_c}{2M} \tag{2}$$

where $M = \sum_{i=1}^{n} m_i$ is the total mass of the aggregate. R_{g} was calculated and averaged during the production run where there is no change in the number of molecules involved. The compositions and radii of gyration of the aggregates identified in the bulk-liquid simulations are reported in Table 1. With 2.5 wt% PIBSA-PAM and 7.5 wt% GMO, a cluster contains around 8 molecules of GMO and 2 molecules of PIBSA-PAM, and it is very diffuse, hence the large value of R_{g}. With 10.0 wt% GMO, the aggregate is a compact and well-defined reverse micelle containing about 12 molecules.

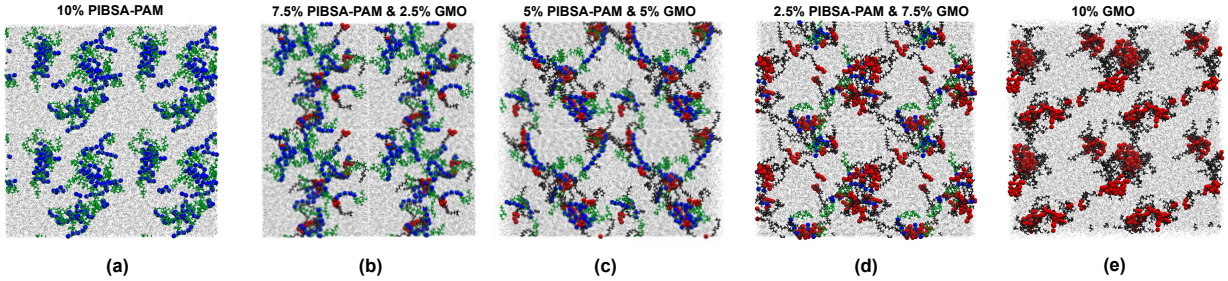

Figure 2: Snapshots for five systems at $P = 1$ atm and $T = 298.15$ K: (a) 10.0 wt% PIBSA-PAM; (b) 7.5 wt% PIBSA-PAM and 2.5 wt% GMO; (c) 5.0 wt% PIBSA-PAM and 5.0 wt% GMO; (d) 2.5 wt% PIBSA-PAM and 7.5 wt% GMO; (e) 10.0 wt% GMO. Four periodic replicas of the central simulation cell are shown. The PIBSA-PAM molecules are represented as green chains, with the nitrogen atoms highlighted as blue spheres, and the GMO molecules are represented as gray chains, with oxygens atoms highlighted as red spheres.

Figure 3 shows a large aggregate from the simulation with 2.5 wt% PIBSA-PAM and 7.5 wt% GMO. Figure 3(a) shows the atoms in space-filling representation, and this highlights the extent to which the non-polar tails on both types of additive molecule shield the polar head groups from the solvent. To show the polar core of the aggregate, Figure 3(b) shows the molecules in a ball-and-stick representation, with the electronegative N and O atoms shown

as spheres, and the tails as sticks. This shows the extent of clustering of the solvophobic, polar head groups within the aggregate, which underlines why self-assembly can compete with physisorption on surfaces.

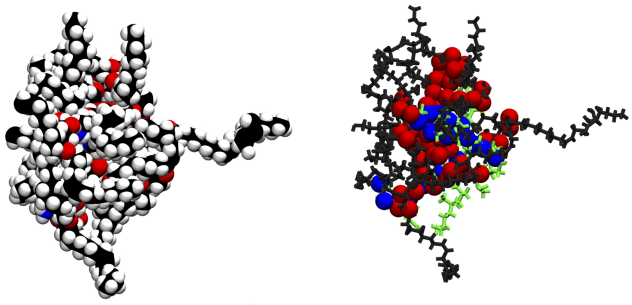

Figure 3: Snapshot of a large aggregate from the simulation with 2.5 wt% PIBSA-PAM and 7.5 wt% GMO. (a) Space-filling representation. The atoms are shown according to the standard CPK scheme: hydrogen is white; carbon is black; nitrogen is blue; and oxygen is red. (b) Ball-and-stick representation. The PIBSA-PAM molecules are represented as green chains, with the nitrogen atoms highlighted as blue spheres, and the GMO molecules are represented as gray chains, with oxygens atoms highlighted as red spheres.

3.2 Self-assembly under confinement and static conditions

The structures of the same five systems confined between two iron-oxide slabs, at pressure $P = 1$ atm and a higher temperature of 313 K, are illustrated in Figure 4. For each system, a snapshot and the average mass-density profiles $\rho(z)$ are shown. With 5 wt% GMO, there is adsorption of both additives, with a few molecules in the liquid layer. With higher GMO content, there is both adsorption and self-assembly of the GMO, with any PIBSA-PAM associated primarily in the GMO aggregate. The snapshots indicate that the larger aggregates are not strongly adsorbed onto the surfaces. This is understandable, because the non-polar moieties of the additives are on the outside of the aggregates, they will not have a strong attraction to the iron-oxide surfaces, and they have more conformational freedom

when surrounded by liquid.

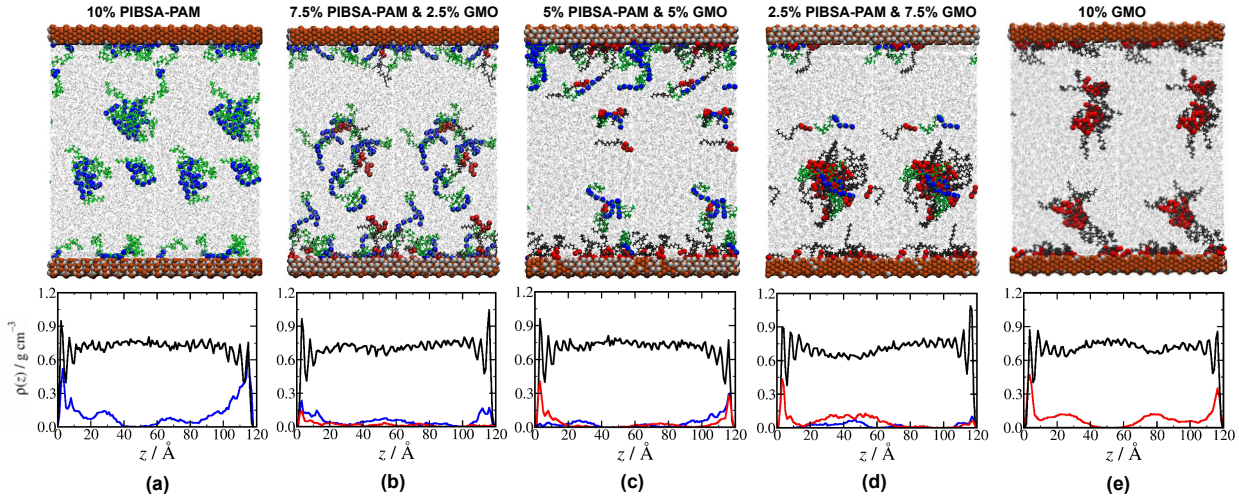

Figure 4: Snapshots and density profiles for systems confined between iron-oxide slabs at $P = 1$ atm and $T = 313$ K: (a) 10.0 wt% PIBSA-PAM; (b) 7.5 wt% PIBSA-PAM and 2.5 wt% GMO; (c) 5.0 wt% PIBSA-PAM and 5.0 wt% GMO; (d) 2.5 wt% PIBSA-PAM and 7.5 wt% GMO; (e) 10.0 wt% GMO. Two periodic replicas are shown. In the snapshots, the PIBSA-PAM molecules are represented as green chains, with the nitrogen atoms highlighted as blue spheres, and the GMO molecules are represented as gray chains, with oxygens atoms highlighted as red spheres. In the density profiles, the black lines are for squalane, the blue lines are for PIBSA-PAM, and the red lines are for GMO.

The mass-density profiles are shown separately for PIBSA-PAM, GMO, and squalane as a function of 'height' z, with $z = 0$ at the bottom of the liquid layer, and $z = H$ at the top of the liquid layer. Firstly, the squalane shows considerable layering near the iron-oxide surfaces, with the peaks separated by a distance corresponding to the diameters of CH, CH_2, and CH_3 groups. This is typical for any liquid – atomic or molecular – near a hard surface. Secondly, the density profiles for PIBSA-PAM and GMO clearly show the coexistence of adsorbed and solvated/self-assembled molecules. The profiles confirm that self-assembly is significant when the GMO content is high, but that there is a degree of surface adsorption in all cases. Finally, note that the self-assembly is maximized in the system with 7.5 wt%

GMO. Some tests were done at higher pressures of $P = 10^3$ and 10^4 atm, but there was no change in the adsorption and self-assembly under static conditions.

3.3 Self assembly under confinement and shear conditions

Figure 5 shows results for systems confined and sheared between iron-oxide slabs with relative sliding velocity $v_s = 10$ m s^{-1}, and at pressure $P = 10^3$ atm and temperature $T = 353$ K. The most significant structural changes on increasing the pressure, temperature, and shear are that with 7.5 wt% GMO, the combined PIBSA-PAM/GMO aggregate remains mainly intact, while with 10 wt% GMO, the aggregates have either disintegrated or adsorbed onto the surfaces, but overall the adsorption has increased. At all of the other compositions, the changes are minimal. The mass-density profiles help quantify these changes. For instance, with 10 wt% GMO, the distinct peaks in the liquid layer seen under static conditions [Figure 4(e)] are much reduced under shear conditions, and the GMO peaks near the iron-oxide surfaces increase on shear.

Figure 5 also shows velocity profiles, $v_x(z)$. In the ideal case of a fluid showing no slip or stick near the walls, the velocity profile would be perfectly linear and described by $v_x(z) = \dot{\gamma}(z - z_0)$, where $\dot{\gamma} = v_s/H$ is the shear rate, and $z_0 = H/2$ is the midpoint of the fluid layer. In reality, adsorption and self-assembly of the additive molecules, as well as the layering of the solvent near the surfaces, significantly disrupt the velocity profiles. Figure 5 shows both the measured and the ideal velocity profiles. In each case, the measured velocity profile does show linear behavior away from the surfaces, and this portion of the profile can be fitted with an equation

$$v_x(z) = \dot{\gamma}_{\text{eff}}\,(z - z_0) \tag{3}$$

where $\dot{\gamma}_{\text{eff}}$ is an effective shear rate. From this kind of fit, it is possible to define a stick or

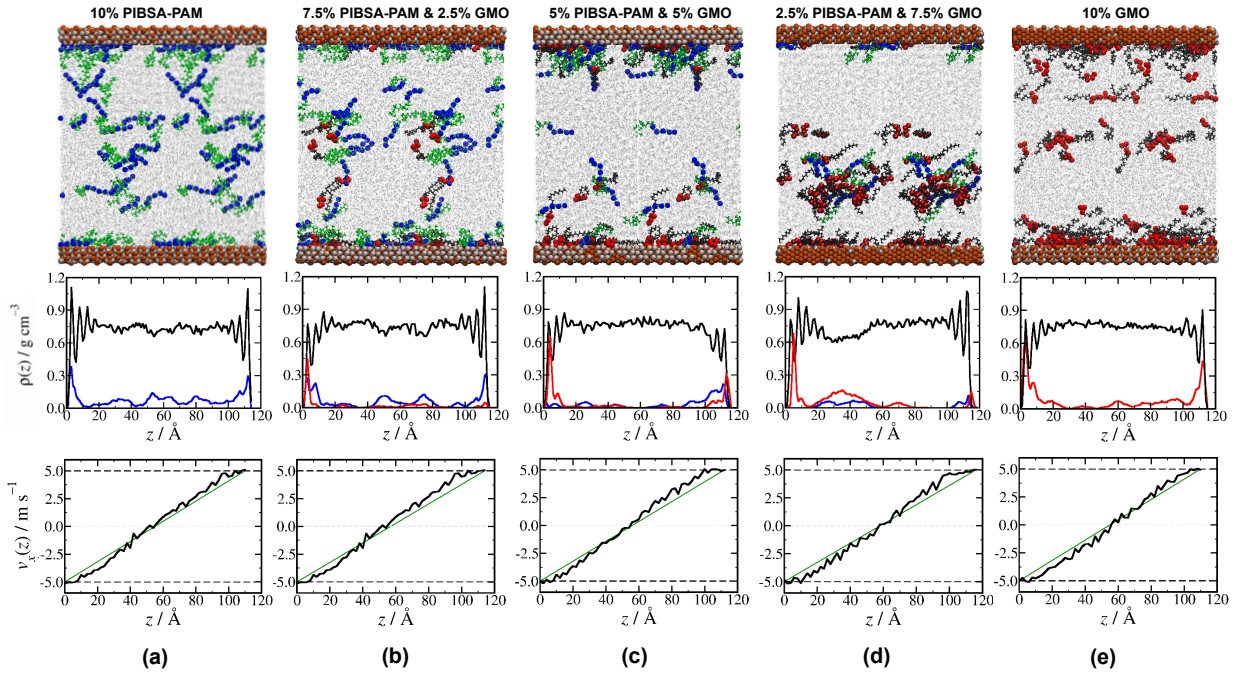

Figure 5: Snapshots, mass-density profiles, and velocity profiles for systems confined and sheared between iron-oxide slabs with relative sliding speed $v_s = 10$ m s^{-1}, and at $P = 10^3$ atm and $T = 353$ K: (a) 10.0 wt% PIBSA-PAM; (b) 7.5 wt% PIBSA-PAM and 2.5 wt% GMO; (c) 5.0 wt% PIBSA-PAM and 5.0 wt% GMO; (d) 2.5 wt% PIBSA-PAM and 7.5 wt% GMO; (e) 10.0 wt% GMO. Two periodic replicas are shown. In the snapshots, the PIBSA-PAM molecules are represented as green chains, with the nitrogen atoms highlighted as blue spheres, and the GMO molecules are represented as gray chains, with oxygens atoms highlighted as red spheres. In the density profiles, the black lines are for squalane, the blue lines are for PIBSA-PAM, and the red lines are for GMO. In the velocity profiles, the black lines are the simulation results, the green lines are the ideal, no-slip/stick profiles $[v_x(z) = v_s(z/H - 1/2)]$, and the dashed lines are the sliding velocities $\pm v_s/2$.

slip length describing the velocity profile near the surfaces, by determining the value of z where the extrapolated linear portion of the velocity profile would equal the sliding speed of the wall.

$$v_x(z_\pm) = \dot{\gamma}_{\rm eff}\,(z_\pm - z_0) = \pm\frac{1}{2}v_{\rm s} \tag{4}$$

From this condition, the differences between $z_\pm$ and the surfaces (at $z = 0$ and H) can be identified with stick/slip lengths $\lambda_\pm$ at the top and bottom surfaces.

$$\lambda_+ \;=\; z_+ - H = \frac{v_{\rm s}}{2\dot{\gamma}_{\rm eff}} + z_0 - H \tag{5}$$

$$\lambda_- \;=\; 0 - z_- = \frac{v_{\rm s}}{2\dot{\gamma}_{\rm eff}} - z_0 \tag{6}$$

In the ideal case, $\dot{\gamma}_{\rm eff} = \dot{\gamma} = v_{\rm s}/H$ and $z_0 = H/2$, and so $\lambda_\pm = 0$. If there is slip at the solid-liquid interface, then $\dot{\gamma}_{\rm eff} < \dot{\gamma}$, and $\lambda_\pm > 0$. If there is a layer of the liquid that adsorbs at the solid surface, then $\dot{\gamma}_{\rm eff} > \dot{\gamma}$, and $\lambda_\pm < 0$. Hence $\lambda_\pm$ should give a simple indication of how the liquid adsorbs at the solid surface and modifies the velocity profile. Figure 5 shows linear fits along with the measured and ideal velocity profiles. In all cases, $\dot{\gamma}_{\rm eff} > \dot{\gamma}$ meaning that there is adsorption, and hence stick, at the solid-liquid interface. The apparent stick lengths are reported in Table 2, along with the average liquid-layer thickness H, the ideal and fitted shear rates $\dot{\gamma}$ and $\dot{\gamma}_{\rm eff}$, respectively, and the position z_0 where $v_x = 0$. In all cases, z_0 is close to the center of the liquid layer. The average stick length is $(\lambda_+ + \lambda_-)/2 \simeq -12$ Å, and the asymmetry is due to random adsorption on the surfaces, and the average position of any aggregates, during the simulation run; there is no physical reason why one surface should show more adsorption than the other.

The kinetic friction coefficient was measured as a function of shear rate $\dot{\gamma}$. Values of μ at a sliding velocity of $v_{\rm s} = 10$ m s^{-1} (corresponding to $\dot{\gamma} \simeq 1 \times 10^9$ s^{-1}) are given in

Table 2: Properties of systems confined and sheared between iron-oxide surfaces with sliding velocity $v_s = 10\ \mathrm{m\ s^{-1}}$, pressure $P = 10^3$ and 10^4 atm, and temperature $T = 353$ K. H is the average separation between the iron-oxide surfaces, $\dot{\gamma} = v_s/H$ is the ideal shear rate, $\dot{\gamma}_{\mathrm{eff}}$ is the effective shear rate, z_0 is the position where $v_x = 0$, λ_+ and λ_- are the stick lengths at the upper and lower surfaces, respectively, and μ is the kinetic friction coefficient. The figures in brackets are the estimated uncertainties in the final digits.

wt% GMO	H/Å	$\dot{\gamma}/10^9\ \mathrm{s^{-1}}$	$\dot{\gamma}_{\mathrm{eff}}/10^9\ \mathrm{s^{-1}}$	$(z_0 - H/2)$/Å	λ_+/Å	λ_-/Å	μ
			$P = 10^3$ atm				
0.00	115.6(1)	0.8649(21)	1.092(17)	0.09(10)	−11.95(81)	−12.13(81)	0.146(26)
2.50	115.9(1)	0.8630(22)	1.079(18)	−3.94(11)	−15.54(78)	−7.66(78)	0.136(26)
5.00	115.7(1)	0.8645(21)	1.098(15)	−3.14(09)	−15.44(63)	−9.16(63)	0.131(26)
6.25	115.9(1)	0.8678(25)	1.079(19)	−3.95(11)	−15.98(87)	−8.10(87)	0.126(26)
7.50	116.1(1)	0.8610(21)	1.088(20)	1.84(13)	−10.27(85)	−13.96(85)	0.124(26)
8.75	116.9(1)	0.8644(22)	1.005(15)	5.36(04)	−3.34(82)	−14.05(82)	0.126(22)
10.00	115.3(1)	0.8674(22)	1.089(18)	1.52(11)	−10.21(77)	−13.25(77)	0.155(26)
			$P = 10^4$ atm				
0.00	98.1(1)	1.0193(23)	1.456(35)	−0.92(11)	−15.63(83)	−13.79(83)	0.138(3)
2.50	98.0(1)	1.0204(24)	1.355(26)	−1.26(14)	−13.36(72)	−10.84(72)	0.135(3)
5.00	98.5(1)	1.0153(23)	1.334(23)	−3.97(12)	−15.74(66)	−7.79(66)	0.134(3)
6.25	98.6(1)	1.1991(19)	1.354(13)	−1.23(08)	−13.62(44)	−11.15(44)	0.135(3)
7.50	98.1(1)	1.0193(24)	1.199(15)	3.65(09)	−3.70(53)	−11.00(53)	0.134(3)
8.75	98.7(1)	1.1029(37)	1.103(13)	−3.08(07)	−7.10(61)	−0.94(61)	0.132(3)
10.00	98.5(1)	1.0154(24)	1.459(29)	6.65(17)	−8.32(70)	−21.62(70)	0.150(3)

Table 2, and all values are plotted as a function of $\dot{\gamma}$ in Figure 6(a). Note that, in the first set of simulations, systems with 0.0, 2.5, 5.0, 7.5, and 10.0 wt% GMO were considered. Of these at the highest shear rate, the system with 7.5 wt% GMO has the lowest friction coefficient, and the system with 10 wt% GMO has the highest friction coefficient. The ordering of other compositions is less straightforward, and so Figure 6(b) shows the friction coefficients for $v_s = 10$ m s^{-1} as a function of composition. The data at the original set of compositions indicate that the friction coefficient shows a minimum for a composition of 7.5 wt% GMO. To test this hypothesis, an extra set of simulations was carried out with 6.25 and 8.75 wt% GMO to try and bracket the optimum composition for minimizing the friction coefficient. The results are shown in Figures 6(a) and (b). These additional results follow the hypothesized trend, showing that μ has a (shallow) minimum centered at around 7.5 wt% GMO.

The snapshots and respective density and velocity profiles of the two new systems with 6.25 and 8.75 wt% GMO are shown in Figure 7. The extra simulations confirm that strong aggregation is correlated with low friction. Due to the proximity of the values and the large error bars in μ, it can be concluded that friction is indeed minimized in the systems containing 6.25–8.25 wt% GMO.

A comment is due about the magnitude of the shear rates. In engineering terms, 10^9 s^{-1} is an immense shear rate. If two smooth surfaces separated by one micron are sheared at 1 m s^{-1}, then the shear rate is 10^6 s^{-1}. But molecular additives control friction and wear at asperity contacts. The thickness of an adsorbed layer of molecules is on the order of 10 Å; this can be seen in Figures 4 and 5. For other surfactants that form monolayers, such as stearic acid, oleic acid, and hexadecylamine, the adsorbed-layer thickness is in the region of 15–20 Å.[20,21,44] The liquid layers can be on the order of nanometers thick – here about 100 Å

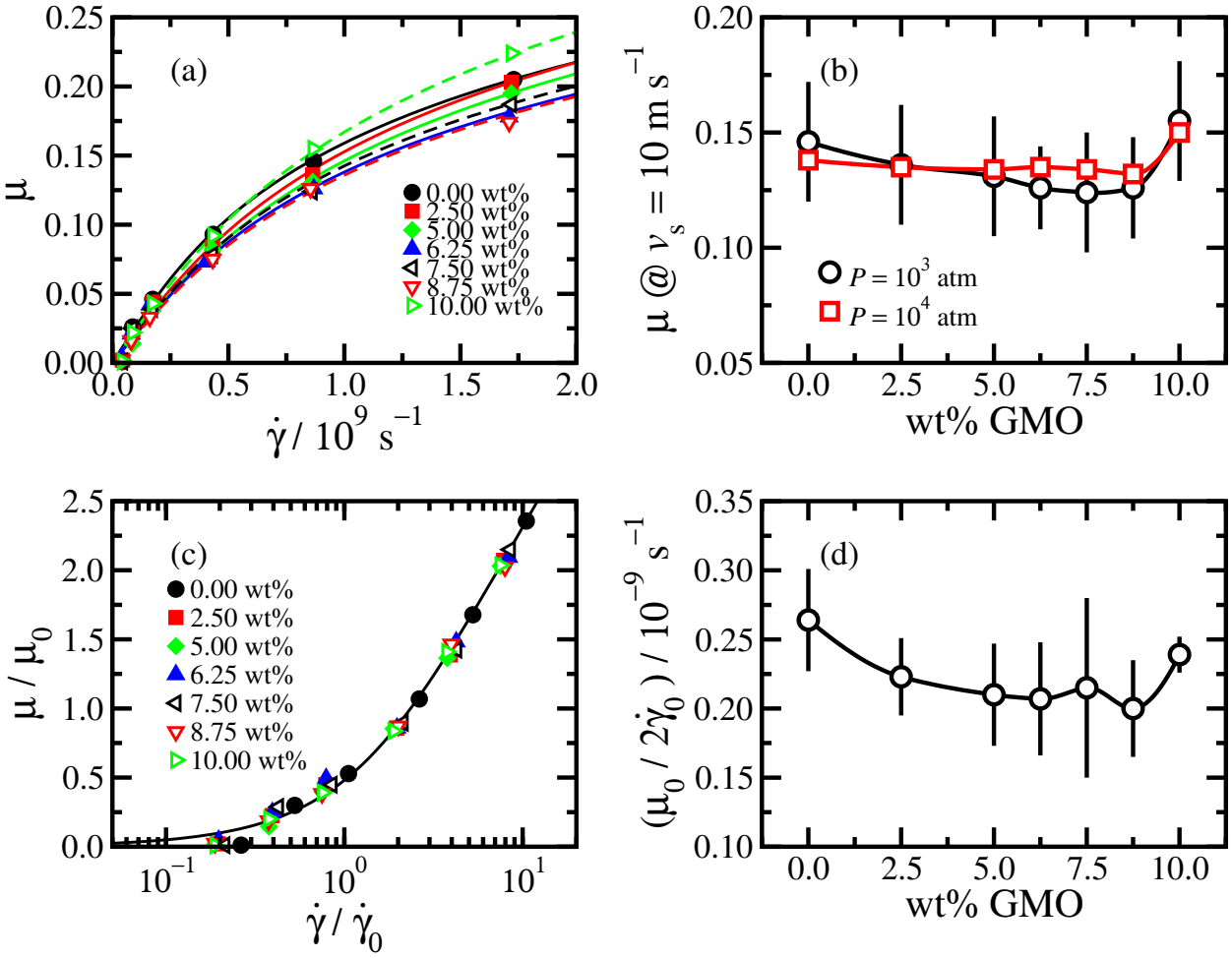

Figure 6: Frictional properties of systems confined and sheared between iron-oxide slabs at $T = 353$ K. (a) Friction coefficients μ against shear rate $\dot{\gamma}$ for systems at $P = 10^3$ atm. The points are from simulations and the curves are fits using Equation (7). (b) Friction coefficient at sliding velocity $v_s = 10$ m s^{-1} ($\dot{\gamma} \simeq 1 \times 10^9$ s^{-1}) as a function of composition for systems at $P = 10^3$ atm (black circles) and $P = 10^4$ atm (red squares). The lines are Akima splines. (c) Universal plot of friction coefficient against shear rate, according to Equation (7), with the fit parameters given in Table 3 for systems at $P = 10^3$ atm. (d) Initial linear slope $\mu_0/2\dot{\gamma}_0$ as a function of composition for systems at $P = 10^3$ atm. The line is an Akima spline.

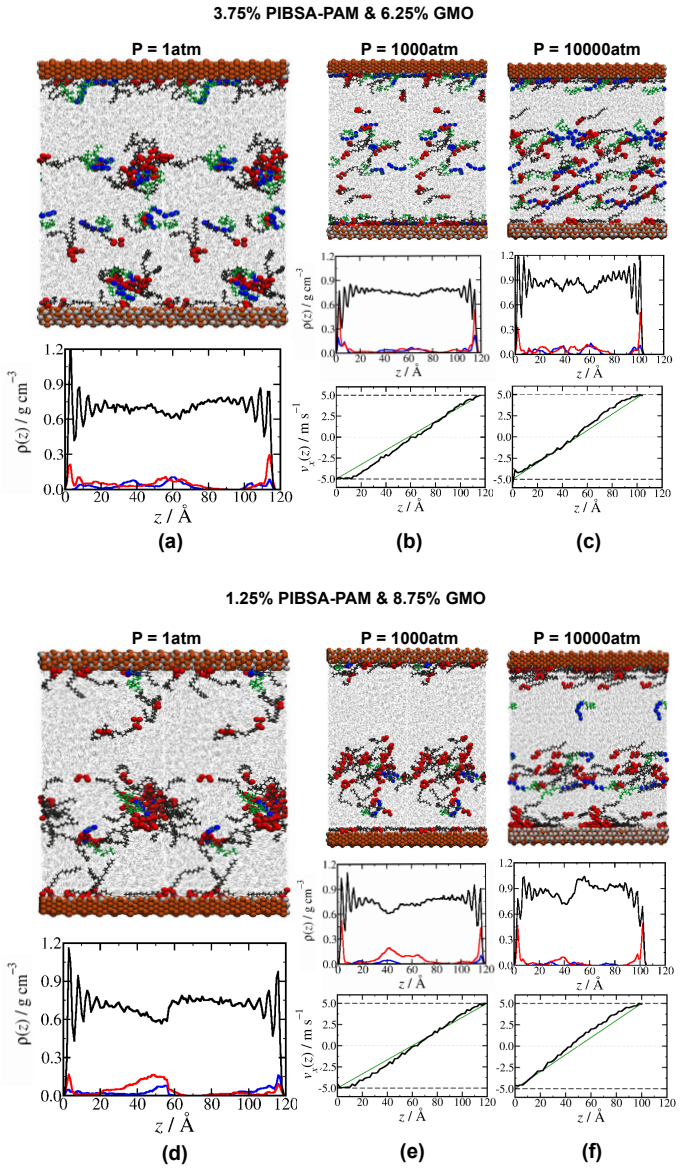

Figure 7: Snapshots, mass-density profiles, and velocity profiles for the additional systems, 3.75 wt% PIBSA-PAM and 6.25 wt% GMO (top), and 1.25 wt% PIBSA-PAM and 8.75 wt% GMO (bottom), under confinement and the following conditions: (a) and (d) $P = 1$ atm, $T = 313$ K, and static conditions; (b) and (e) $P = 10^3$ atm, $T = 353$ K, and $v_s = 10$ m s^{-1}; (c) and (f) $P = 10^4$ atm, $T = 353$ K, and $v_s = 10$ m s^{-1}. Two periodic replicas are shown. In the snapshots, the PIBSA-PAM molecules are represented as green chains, with the nitrogen atoms highlighted as blue spheres, and the GMO molecules are represented as gray chains, with oxygens atoms highlighted as red spheres. In the density profiles, the black lines are for squalane, the blue lines are for PIBSA-PAM, and the red lines are for GMO. In the velocity profiles, the black lines are the simulation results, the green lines are the ideal, no-slip/stick profiles [$v_x(z) = v_s(z/H - 1/2)$], and the dashed lines are the sliding velocities $\pm v_s/2$.

– and so the local shear rates can be much higher than one would estimate from engineering parameters.

Figure 6(a) shows that at high shear rates, the friction coefficient increases logarithmically with shear rate,[1,3,20,40,41,58–65] and this can be described by a very simple theory, which treats the response of the liquid to a shear force in the framework of an Eyring-like, thermally activated hopping theory. The resulting equation for the friction coefficient is[20]

$$\mu = \mu_0 \ln \left[\left(\frac{\dot{\gamma}}{2\dot{\gamma}_0} \right) + \sqrt{1 + \left(\frac{\dot{\gamma}}{2\dot{\gamma}_0} \right)^2} \right] \tag{7}$$

where μ_0 and $\dot{\gamma}_0$ are fitting parameters. At very low shear rates, $\dot{\gamma} \ll \dot{\gamma}_0$, $\mu \approx \mu_0 \dot{\gamma}/2\dot{\gamma}_0$, meaning that μ increases linearly. At very high shear rates, $\dot{\gamma} \gg \dot{\gamma}_0$, $\mu \approx \mu_0 \ln(\dot{\gamma}/\dot{\gamma}_0)$, showing the logarithmic dependence. Therefore, $\dot{\gamma}_0$ is essentially a characteristic shear rate separating the linear and logarithmic regimes. The fits to the simulation data shown in Figure 6(a) are excellent, and the fit parameters are given in Table 3. Figure 6(c) shows a universal, log-linear plot of μ/μ_0 as a function of $\dot{\gamma}/\dot{\gamma}_0$, and the collapse of the data onto the universal curve is excellent. Another measure of friction is the initial, low-shear linear slope, given by $\mu_0/2\dot{\gamma}_0$. This parameter is reported in Table 3 and plotted as a function of composition in Figure 6(d). As the plot shows, the data support the claim that the low-shear friction coefficient is minimized for a system containing both PIBSA-PAM and GMO. Various functions can be fitted to these data to yield the apparent minimum. Figures 6(b) and (d) show interpolations from an Akima spline fit.[66] There is no reason why the minima in the two plots should coincide with one another, as they are each representing different things, but any case, the friction coefficient is minimized when there is a mixture of additives, and there is an excess of GMO (7–8 wt% GMO and 2–3 wt% PIBSA-PAM).

Note that although the estimated errors in μ and $\mu_0/2\dot{\gamma}_0$ are quite large, the results from all of these completely independent runs lie on smooth curves, which gives us confidence in the trends. Although the changes in friction with composition may seem small, being around 10–20%, this would be extremely significant in terms of the global impact of engines; in the UK alone, a 10% increase in fuel economy would decrease fuel consumption by about 4 million liters per day,[67] and decrease CO_2 emissions by about 0.1 Gt per year.[68]

Table 3: Fit parameters from Equation (7) for systems confined and sheared between iron-oxide slabs at $P = 10^3$ atm and $T = 353$ K. The figures in brackets are the estimated uncertainties in the final digits.

wt% GMO	μ_0	$\dot{\gamma}_0/10^9$ s^{-1}	$(\mu_0/2\dot{\gamma}_0)/10^{-9}$ s
0.00	0.087(05)	0.165(21)	0.264(37)
2.50	0.098(06)	0.220(24)	0.223(28)
5.00	0.096(08)	0.229(36)	0.210(37)
6.25	0.085(08)	0.205(36)	0.207(41)
7.50	0.087(12)	0.202(54)	0.215(65)
8.75	0.086(04)	0.215(36)	0.200(35)
10.00	0.110(03)	0.230(11)	0.239(13)

The minimum in the friction coefficient at around 7–8 wt% GMO is correlated with the presence of self-assembled aggregates and a slightly higher average surface separation H; see Table 2. For a given sliding velocity, a higher value of H would lead to a lower value of the shear rate, but the changes are insufficient to explain the drop in friction. The results in Table 2 show that H varies by less than 1%, and hence if shear rate were the primary factor, the friction coefficient would also vary by less than 1%, in both the linear and logarithmic regimes.

It therefore appears that low friction is connected primarily with there being self-assembled aggregates and some adsorption onto the surfaces. Referring back to Figure 5, there is very little self-assembly when the GMO content is low (less than 5 wt%), clearly defined aggregates

in the system with 7.5 wt% GMO, and mainly surface adsorption in the system with 10 wt% GMO, even though the adsorbed GMO forms a surface micelle or hemi-micelle. The essential structural feature for friction reduction is therefore that the additive has self-assembled but has not strongly adsorbed on the surfaces.

To explore this correlation a little further, some simulations were done at a higher load corresponding to a pressure $P = 10^4$ atm, and with a single sliding velocity $v_s = 10$ m s^{-1}. Figure 8 shows snapshots, density profiles, and velocity profiles for systems with five different compositions. The load is now so high that the squalane is close to the point where it no longer acts as a hydrostatic medium, at least under quiescent conditions. Experimentally determined correlations show that at $P = 10^3$ and 10^4 atm and 298.15 K, the shear viscosity is $\eta \simeq 0.2$ and 10^{15} Pa s, respectively.[55] As a result, it is difficult to ensure that the system has reached a steady non-equilibrium state. With that caveat in mind, the results are consistent with those obtained at lower pressure. The system with 7.5 wt% GMO still shows some structuring, but it is no longer in the form of well-defined reverse micelles. Instead, the additives have formed a dense layer due to the extreme pressure and shear. Roughly speaking, the structures of the liquids with other compositions look qualitatively in line with those at lower pressure, and overall, there is less structural variation across the full composition range. Whether the additive molecules are adsorbed or not, they show some orientational ordering along the shear-flow direction. This is caused by the high shear stresses mediated by the solvent, forcing the surfactant molecules to align with the flow. The mass-density and velocity profiles show some interesting effects. With PIBSA-PAM only, the additive molecules appear to form layers within the liquid, giving peaks in the mass-density profile. The velocity profile shows considerable stick at the solid surfaces. With 2.5 wt% GMO, the layering and boundary stick are a bit less pronounced. With 5.0 wt% GMO and above,

the velocity profiles are irregular, showing that there is more stick on one surface than the other. The system with 10 wt% GMO is an extreme example, where the additive forms an extended structure emanating from the bottom surface, and that is where the amount of stick is greatest. These observations are borne out by the stick lengths, which are presented in Table 2. The friction coefficients are given in Table 2 and plotted in Figure 6(b). The variation of μ with composition at 10^4 atm is slightly less pronounced than at 10^3 atm, mirroring the greater similarity between the steady-state structures in the liquid layers. For a given composition, the friction coefficient does not change dramatically on increasing the pressure, which is broadly in line with the Amontons-Coulomb law.

4 Conclusions

In this work, MD simulations were performed to explore the properties and interactions of two common lubricant additives, GMO and PIBSA-PAM, in squalane, both as a bulk liquid, and as a liquid layer confined between iron-oxide surfaces. Lubricant formulations typically contain a dozen or so different components, and while in-depth scientific work may focus on each additive in isolation, it is also important to understand the interactions and any cooperativity between different additives. As a start in that direction, this work was focused on two very important types of lubricant additive. GMO is a widely used friction modifier, and PIBSA-PAM is a common dispersant of soot etc. In all systems, the total concentration of additive in squalane was 10 wt%.

The structural and frictional properties of the compounds in squalane were thoroughly studied. In the bulk liquid at ambient pressure and temperature, the surfactants form aggregates when the GMO is at a concentration of 7.5 wt% or higher. At all other compositions, there is no evidence of self-assembly. Very similar behavior is observed when the liquid is con-

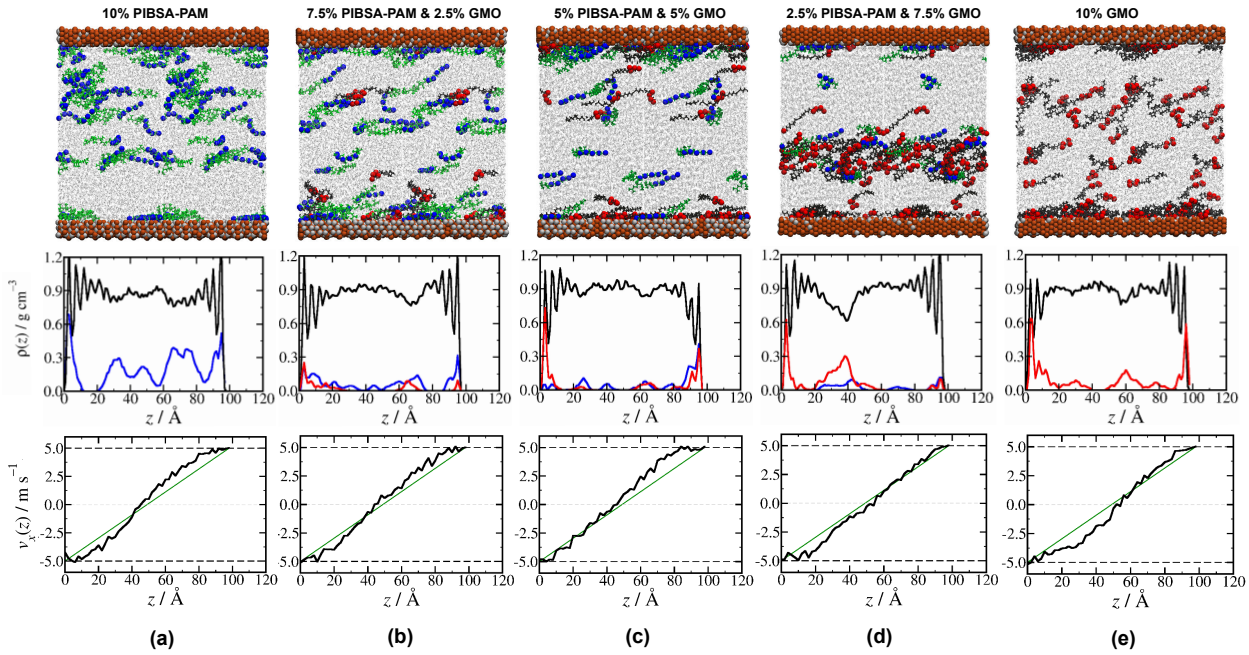

Figure 8: Snapshots, mass-density profiles, and velocity profiles for systems confined and sheared between iron-oxide slabs with relative sliding speed $v_s = 10$ m s^{-1}, and at $P = 10^4$ atm and $T = 353$ K: (a) 10.0 wt% PIBSA-PAM; (b) 7.5 wt% PIBSA-PAM and 2.5 wt% GMO; (c) 5.0 wt% PIBSA-PAM and 5.0 wt% GMO; (d) 2.5 wt% PIBSA-PAM and 7.5 wt% GMO; (e) 10.0 wt% GMO. Two periodic replicas are shown. In the snapshots, The PIBSA-PAM molecules are represented as green chains, with the nitrogen atoms highlighted as blue spheres, and the GMO molecules are represented as gray chains, with oxygens atoms highlighted as red spheres. In the density profiles, the black lines are for squalane, the blue lines are for PIBSA-PAM, and the red lines are for GMO. In the velocity profiles, the black lines are the simulation results, the green lines are the ideal, no-slip/stick profiles $[v_x(z) = v_s(z/H - 1/2)]$, and the dashed lines are the sliding velocities $\pm v_s/2$.

fined between two iron-oxide surfaces, and held under near-ambient conditions, except that there is some adsorption at the solid-liquid interface. To simulate the conditions found in engines, the system was then put under loads equivalent to 10^3 or 10^4 atm, heated to a realistic operating temperature of 353 K, and subjected to shear. In systems at 10^3 atm and where there was no self-assembly, such as at low GMO content, molecules simply remained either fully solvated or adsorbed on the surfaces. With 7.5 wt% GMO, large aggregates remained intact, while with 10.0 wt% GMO, aggregates partially disintegrated and/or adsorbed on a surface. The kinetic friction was observed to be lowest when there was a slight excess of GMO. The optimum composition is in the region of 7–8 wt% GMO and 2–3 wt% PIBSA-PAM, where both the friction coefficient at high shear, and the low-shear linear slope in friction coefficient, are minimized. This composition range is precisely where self-assembled structures are robust to the application of shear. At 10^4 atm, the variation in friction coefficient is much less pronounced, mirroring the relatively weak variations in steady-state structure in the liquid layer under shear, and the disintegration of self-assembled structures.

In the medium-term, internal combustion engines will be designed around low-viscosity base oils, in order to improve fuel efficiency. The qualitative phenomena reported herein are expected to occur in lighter hydrocarbon solvents; self-assembly of lubricant additives, and strong correlations with friction, have also been predicted in solvents such as *n*-heptane and toluene.[39–41] For a given shear rate, the shear stresses are lower in a lower-viscosity solvent, and hence the effects on additive self-assembly and aggregate break-up would be shifted to higher shear rates. But for applications in engines, this may not have any material effect, because the shear rates studied here are so high. Therefore, the current work on additive interactions, self-assembly, adsorption, and friction may well apply to future generations of base oils. This exploratory study shows that cooperative interactions may be significant, and

therefore should be considered when designing complex lubricant formulations containing many interacting components.

Acknowledgement

This research project was supported through a studentship to GT funded by BP International Ltd. [Research Agreement GPTL/92534(2)], and access to computational resources at the BP Center for High-Performance Computing in Houston, Texas.

References

(1) Hardy, W.; Bircumshaw, I. Boundary Lubrication. Plane Surfaces and the Limitations of Amontons' Law. *Proc. R. Soc. Lond. A* **1925**, *108*, 1–27.

(2) Bowden, F. P.; Gregory, J. N.; Tabor, D. Lubrication of Metal Surfaces by Fatty Acids. *Nature* **1945**, *156*, 97–101.

(3) Bowden, F. P.; Tabor, D. *The Friction and Lubrication of Solids*, revised ed.; Oxford University Press, 2001.

(4) Pawlak, Z. Tribochemistry of Lubricating Oils. Tribology and Interface Engineering Series. Amsterdam, 2003; pp 1–368.

(5) Mortier, R. M.; Malcolm, F.; Orszulik, S. *Chemistry and Technology of Lubricants*; Springer: Dordrecht, 2010.

(6) Ewen, J. P.; Heyes, D. M.; Dini, D. Advances in Nonequilibrium Molecular Dynamics Simulations of Lubricants and Additives. *Friction* **2018**, *6*, 349–386.

(7) Greenfield, M. L.; Ohtani, H. Molecular Dynamics Simulation Study of Model Friction Modifier Additives Confined Between Two Surfaces. *Tribol. Lett.* **1999**, *7*, 137–145.

(8) Bair, S.; McCabe, C.; Cummings, P. T. Comparison of Nonequilibrium Molecular Dynamics with Experimental Measurements in the Nonlinear Shear-Thinning Regime. *Phys. Rev. Lett.* **2002**, *88*, 058302.

(9) Cui, S. T.; McCabe, C.; Cummings, P. T.; Cochran, H. D. Molecular Dynamics Study of the Nano-Rheology of *n*-Dodecane Confined Between Planar Surfaces. *J. Chem. Phys.* **2003**, *118*, 8941–8944.

(10) Sivebaek, I. M.; Samoilov, V. N.; Persson, B. N. J. Velocity Dependence of Friction of Confined Hydrocarbons. *Langmuir* **2010**, *26*, 8721–8728.

(11) Sivebaek, I. M.; Samoilov, V. N.; Persson, B. N. J. Effective Viscosity of Confined Hydrocarbons. *Phys. Rev. Lett.* **2012**, *108*, 036102.

(12) Zheng, X.; Zhu, H.; Tieu, A. K.; Chen, K. Molecular Dynamics Simulation of Confined *n*-Alkanes: Ordered Structure and Crystalline Bridges. *Int. J. Surface Science and Engineering* **2014**, *8*, 201–212.

(13) Porras-Vazquez, A.; Martinie, L.; Vergne, P.; Fillot, N. Independence Between Friction and Velocity Distribution in Fluids Subjected to Severe Shearing and Confinement. *Phys. Chem. Chem. Phys.* **2018**, *20*, 27280–27293.

(14) Jadhao, V.; Robbins, M. O. Rheological Properties of Liquids Under Conditions of Elastohydrodynamic Lubrication. `https://arxiv.org/abs/1903.03996v1`, 2019.

(15) Gupta, S. A.; Cochran, H. D.; Cummings, P. T. Shear Behavior of Squalane and Tetracosane Under Extreme Confinement. III. Effect of Confinement on Viscosity. *J. Chem. Phys.* **1997**, *107*, 10335–10343.

(16) Rivera, J. L.; Jennings, G. K.; McCabe, C. Examining the Frictional Forces Between Mixed Hydrophobic-Hydrophilic Alkylsilane Monolayers. *J. Chem. Phys.* **2012**, *136*, 244701.

(17) Lundgren, S. M.; Ruths, M.; Danerlöv, K.; Persson, K. Effects of Unsaturation on Film Structure and Friction of Fatty Acids in a Model Base Oil. *J. Colloid Interface Sci.* **2008**, *326*, 530–536.

(18) Ruths, M.; Lundgren, S.; Danerlöv, K.; Persson, K. Friction of Fatty Acids in Nanometer-Sized Contacts of Different Adhesive Strength. *Langmuir* **2008**, *24*, 1509–1516.

(19) Eder, S.; Vernes, A.; Betz, G. On the Derjaguin Offset in Boundary-Lubricated Nanotribological Systems. *Langmuir* **2013**, *29*, 13760–13772.

(20) Doig, M.; Warrens, C. P.; Camp, P. J. Structure and Friction of Stearic Acid and Oleic Acid Films Adsorbed on Iron-Oxide Surfaces in Squalane. *Langmuir* **2014**, *30*, 186–195.

(21) Doig, M.; Camp, P. J. The Structures of Hexadecylamine Films Adsorbed on Iron-Oxide Surfaces in Dodecane and Hexadecane. *Phys. Chem. Chem. Phys.* **2015**, *17*, 5248–5255.

(22) Ewen, J. P.; Gattinoni, C.; Morgan, N.; Spikes, H. A.; Dini, D. Nonequilibrium Molecular Dynamics Simulations of Organic Friction Modifiers Adsorbed on Iron Oxide Surfaces. *Langmuir* **2016**, *32*, 4450–4463.

(23) Ewen, J. P.; Gattinoni, C.; Thakkar, F. M.; Morgan, N.; Spikes, H. A.; Dini, D. A Comparison of Classical Force-Fields for Molecular Dynamics Simulations of Lubricants. *Materials* **2016**, *9*, 651–667.

(24) Ewen, J. P.; Restrepo, S. E.; Morgan, N.; Dini, D. Nonequilibrium Molecular Dynamics Simulations of Stearic Acid Adsorbed on Iron Surfaces with Nanoscale Roughness. *Tribol. Int.* **2017**, *107*, 264–273.

(25) Jaishankar, A.; Jusufi, A.; Vreeland, J. L.; Deighton, S.; Pellettiere, J.; Schilowitz, A. M. Adsorption of Stearic Acid at the Iron Oxide/Oil Interface: Theory, Experiments, and Modeling. *Langmuir* **2019**, *35*, 2033–2046.

(26) Morita, Y.; Jinno, S.; Murakami, M.; Hatakeyama, N.; Miyamoto, A. A Computational Chemistry Approach for Friction Reduction of Automotive Engines. *Int. J. Engine Res.* **2014**, *15*, 399–405.

(27) Davidson, J. E.; Hinchley, S. L.; Harris, S. G.; Parkin, A.; Parsons, S.; Tasker, P. A. Molecular Dynamics Simulations to Aid the Rational Design of Organic Friction Modifiers. *J. Mol. Graphics Modell.* **2006**, *25*, 495–506.

(28) Berro, H.; Fillot, N.; Vergne, P. Molecular Dynamics Simulation of Surface Energy and ZDDP Effects on Friction in Nano-Scale Lubricated Contacts. *Tribol. Int.* **2010**, *43*, 1811–1822.

(29) Onodera, T.; Morita, Y.; Suzuki, A.; Koyama, M.; Tsuboi, H.; Hatakeyama, N.; Endou, A.; Takaba, H.; Kubo, M.; Dassenoy, F.; Minfray, C.; Joly-Pottuz, L.; Martin, J.-M.; Miyamoto, A. A Computational Chemistry Study on Friction of h-MoS_2. Part I. Mechanism of Single Sheet Lubrication. *J. Phys. Chem. B* **2009**, *113*, 16526–16536.

(30) Onodera, T.; Morita, Y.; Nagumo, R.; Miura, R.; Suzuki, A.; Tsuboi, H.; Hatakeyama, N.; Endou, A.; Takaba, H.; Dassenoy, F.; Minfray, C.; Joly-Pottuz, L.; Kubo, M.; Martin, J.-M.; Miyamoto, A. A Computational Chemistry Study on Friction of h-MoS_2 Part II. Friction Anisotropy. *J. Phys. Chem. B* **2010**, *114*, 15832–15838.

(31) Canova, F. F.; Matsubara, H.; Mizukami, M.; Kurihara, K.; Shluger, A. L. Shear Dynamics of Nanoconfined Ionic Liquids. *Phys. Chem. Chem. Phys.* **2014**, *16*, 8247–8256.

(32) Mendonça, A. C. F.; Pádua, A. A. H.; Malfreyt, P. Nonequilibrium Molecular Simula-

tions of New Ionic Lubricants at Metallic Surfaces: Prediction of the Friction. *J. Chem. Theory Comput.* **2013**, *9*, 1600–1610.

(33) Ewen, J. P.; Gattinoni, C.; Thakkar, F. M.; Morgan, N.; Spikes, H. A.; Dini, D. Nonequilibrium Molecular Dynamics Investigation of the Reduction in Friction and Wear by Carbon Nanoparticles Between Iron Surfaces. *Tribol. Lett.* **2016**, *63*, 1–15.

(34) Pitzalis, P.; Monduzzi, M.; Krog, N.; Larsson, H.; Ljusberg-Wahren, H.; Nylander, T. Characterization of the Liquid-Crystalline Phases in the Glycerol Monooleate/Diglycerol Monooleate/Water System. *Langmuir* **2000**, *16*, 6358–6365.

(35) Shrestha, L. K.; Glatter, O.; Aramaki, K. Structure of Nonionic Surfactant Glycerol α-Monomyristate Micelles in Organic Solvents: A SAXS Study. *J. Phys. Chem. B* **2009**, *113*, 6290–6298.

(36) Shrestha, L. K.; Shrestha, R. G.; Abe, M.; Ariga, K. Reverse Micelle Microstructural Transformations Induced by Oil and Water. *Soft Matter* **2011**, *7*, 10017–10024.

(37) Shrestha, R. G.; Shrestha, L. K.; Ariga, K.; Abe, M. Reverse Micelle Microstructural Transformations Induced by Surfactant Molecular Structure, Concentration, and Temperature. *J. Nanosci. Nanotechno.* **2011**, *11*, 7665–7675.

(38) Shrestha, L. K.; Shrestha, R. G.; Aramaki, K.; Hill, J. P.; Ariga, K. Nonionic Reverse Micelle Formulation and Their Microstructure Transformations in an Aromatic Solvent Ethylbenzene. *Colloids Surf. A* **2012**, *414*, 140–150.

(39) Bradley-Shaw, J. L.; Camp, P. J.; Dowding, P. J.; Lewtas, K. Glycerol Monooleate Reverse Micelles in Nonpolar Solvents: Computer Simulations and Small-Angle Neutron Scattering. *J. Phys. Chem. B* **2015**, *119*, 4321–4331.

(40) Bradley-Shaw, J. L.; Camp, P. J.; Dowding, P. J.; Lewtas, K. Molecular Dynamics Simulations of Glycerol Monooleate Confined Between Mica Surfaces. *Langmuir* **2016**, *32*, 7707–7718.

(41) Bradley-Shaw, J. L.; Camp, P. J.; Dowding, P. J.; Lewtas, K. Self-Assembly and Friction of Glycerol Monooleate and Its Hydrolysis Products in Bulk and Confined Non-Aqueous Solvents. *Phys. Chem. Chem. Phys.* **2018**, *20*, 17648–17657.

(42) Shen, L.; Duhamel, J. Micellization and Adsorption of a Series of Succinimide Dispersants. *Langmuir* **2008**, *24*, 10665–10673.

(43) Diaby, M.; Sablier, M.; Le Negrate, A.; El Fassi, M. Kinetic Study of the Thermo-Oxidative Degradation of Squalane ($C_{30}H_{62}$) Modelling the Base Oil of Engine Lubricants. *Proceedings of the Spring Technical Conference of the ASME Internal Combustion Engine Division* **2009**, *132*, 671–681.

(44) Wood, M. H.; Welbourn, R. J. L.; Charlton, T.; Zarbakhsh, A.; Casford, M. T.; Clarke, S. M. Hexadecylamine Adsorption at the Iron Oxide-Oil Interface. *Langmuir* **2013**, *29*, 13735–13742.

(45) Wood, M. H.; Casford, M. T.; Seitz, R.; Zarbakhsh, A.; Welbourn, R. J. L.; Clarke, S. M. Comparative Adsorption of Saturated and Unsaturated Fatty Acids at the Iron Oxide/Oil Interface. *Langmuir* **2016**, *32*, 534–540.

(46) Chia, C.-L.; Avendaño, C.; Siperstein, F. R.; Filip, S. Liquid Adsorption of Organic Compounds on Hematite α-Fe_2O_3 Using ReaxFF. *Langmuir* **2017**, *33*, 11257–11263.

(47) Gattinoni, C.; Ewen, J. P.; Dini, D. Adsorption of Surfactants on α-Fe_2O_3(0001): A Density Functional Theory Study. *J. Phys. Chem. C* **2018**, *122*, 20817–20826.

(48) Chia, C.-L.; Alloway, R. M.; Jephson, I.; Clarke, S. M.; Filip, S. V.; Siperstein, F. R.; Avendaño, C. Competitive Adsorption of a Multifunctional Amine and Phenol Surfactant with Ethanol on Hematite from Nonaqueous Solution. *J. Phys. Chem. B* **2019**, *123*, 1375–1383.

(49) Sivebaek, I. M.; Samoilov, V. N.; Persson, B. N. J. Squeezing Molecular Thin Alkane Lubrication Films Between Curved Solid Surfaces with Long-Range Elasticity: Layering Transitions and Wear. *J. Chem. Phys.* **2003**, *119*, 2314–2321.

(50) Tartaglino, U.; Sivebaek, I. M.; Persson, B. N. J.; Tosatti, E. Impact of Molecular Structure on the Lubricant Squeeze-Out Between Curved Surfaces with Long Range Elasticity. *J. Chem. Phys.* **2006**, *125*, 014704.

(51) Plimpton, S. Fast Parallel Algorithms for Short-Range Molecular Dynamics. *J. Comp. Phys.* **1995**, *117*, 1–19.

(52) LAMMPS Molecular Dynamics Simulator. `http://lammps.sandia.gov`, 1995.

(53) Jorgensen, W. L.; Madura, J. D.; Swenson, C. J. Optimized Intermolecular Potential Functions for Liquid Hydrocarbons. *J. Am. Chem. Soc.* **1984**, *106*, 6638–6646.

(54) Jorgensen, W. L.; Maxwell, D. S.; Tirado-Rives, J. Development and Testing of the OPLS All-Atom Force Field on Conformational Energetics and Properties of Organic Liquids. *J. Am. Chem. Soc.* **1996**, *118*, 11225–11236.

(55) Mylona, S. K.; Assael, M. J.; Comuñas, M. J. P.; Paredes, X.; Gaciño, F. M.; Fernández, J.; Bazile, J. P.; Boned, C.; Daridon, J. L.; Galliero, G.; Pauly, J.; Harris, K. R. Reference Correlations for the Density and Viscosity of Squalane from 273 to 473 K at Pressures to 200 MPa. *J. Phys. Chem. Ref. Data* **2014**, *43*, 013104.

(56) Blake, R. L.; Hessevick, R. E.; Zoltai, T.; Finger, L. W. Refinement of the Hematite Structure. *Am. Mineral.* **1966**, *51*, 123–129.

(57) Humphrey, W.; Dalke, A.; Schulten, K. VMD – Visual Molecular Dynamics. *J. Mol. Graphics* **1996**, *14*, 33–38.

(58) Dieterich, J. H. Modeling of Rock Friction: 1. Experimental Results and Constitutive Equations. *J. Geophys. Res.* **1979**, *84*, 2161–2168.

(59) Dieterich, J. H. Modeling of Rock Friction: 2. Simulation of Pre-Seismic Slip. *J. Geophys. Res.* **1979**, *84*, 2169–2175.

(60) Briscoe, B. J.; Evans, D. C. B. The Shear Properties of Langmuir-Blodgett Layers. *Proc. R. Soc. Lond. A* **1982**, *380*, 389–407.

(61) Ruina, A. Slip Instability and State Variable Friction Laws. *J. Geophys. Res.* **1983**, *88*, 359–370.

(62) Gu, J. C.; Rice, J. R.; Ruina, A. L.; Tse, S. T. Slip Motion and Stability of a Single Degree of Freedom Elastic System With Rate and State Dependent Friction. *J. Mech. Phys. Sol.* **1984**, *32*, 167–196.

(63) Perez, D.; Dong, Y.; Martini, A.; Voter, A. F. Rate Theory Description of Atomic Stick-Slip Friction. *Phys. Rev. B* **2010**, *81*, 24515.

(64) Campen, S.; Green, J.; Lamb, G.; Atkinson, D.; Spikes, H. On the Increase in Boundary Friction with Sliding Speed. *Tribol. Lett.* **2012**, *48*, 237–248.

(65) Farrow, M. R.; Chremos, A.; Camp, P. J.; Harris, S. G.; Watts, R. F. Molecular Sim-

ulations of Friction Modification in Nanoscale Fluid Layers. *Tribol. Lett.* **2011**, *42*, 325–337.

(66) Akima, H. A New Method of Interpolation and Smooth Curve Fitting Based on Local Procedures. *J. Assoc. Comput. Mach.* **1970**, *17*, 589–602.

(67) UKPIA Statistical Review 2018. `http://www.ukpia.com/docs/default-source/default-document-library/ukpia-statistical-review-2018.pdf`, 2018.

(68) Fulton, L. M. How Vehicle Fuel Economy Improvements Can Save $2 Trillion and Help Fund a Long-Term Transitition to Plug-In Vehicles. Global Fuel Economy Initiative Working Paper 9. `https://www.fiafoundation.org/media/44075/wp9-fuel-economy-improvements.pdf`, 2013.

Graphical TOC Entry